

# Distribution of Gamma-Ray Bursts on the $T_{90}$ – HR plane and Their Classification Revisited

Liang Zhang<sup>1\*</sup>, Juan-Juan Luo<sup>2†</sup>, Yong-Feng Huang<sup>3,4‡</sup>, Yu-Jun Gong<sup>5</sup>, and Sheng Wu<sup>6</sup>

<sup>1</sup>Guizhou Vocational College of Economics and Business, Duyun 558022, P. R. China

<sup>2</sup>School of Physics and Electronics, Qiannan Normal University for Nationalities, Duyun 558000, P. R. China

<sup>3</sup>School of Astronomy and Space Science, Nanjing University, Nanjing 210023, P. R. China

<sup>4</sup>Key Laboratory of Modern Astronomy and Astrophysics (Nanjing University), Ministry of Education, Nanjing 210023, P. R. China

<sup>5</sup>Qiannan Polytechnic for Nationalities, Duyun 558022, P. R. China

<sup>6</sup>Guangzhou Intelligence Communications Technology Co., Ltd, Guangzhou 510630, P. R. China

Accepted XXX. Received YYY; in original form ZZZ

## ABSTRACT

Using four mixed bivariate distributions (*Normal* distribution, *Skew-Normal* distribution, *Student* distribution, *Skew-Student* distribution) and bootstrap re-sampling analysis, we analyze the samples of *CGRO/BATSE*, *Swift/BAT* and *Fermi/GBM* gamma-ray bursts in detail on the  $T_{90}$  – *HR* (Hardness Ratio) plane. The Bayesian information criterion is used to judge the goodness of fit for each sample, comprehensively. It is found that all the three samples show a symmetric (either *Normal* or *Student*) distribution. It is also found that the existence of three classes of gamma-ray bursts is preferred by the three samples, but the strength of this preference varies with the sample size: when the sample size of the data set is larger, the preference of three classes scheme becomes weaker. Therefore, the appearance of an intermediate class may be caused by a small sample size and the possibility that there are only two classes of gamma-ray bursts still cannot be expelled yet. A further bootstrap re-sampling analysis also confirms this result.

**Key words:** gamma-ray bursts: general – methods: data analysis – methods: statistical

## 1 INTRODUCTION

Gamma-ray bursts (GRBs; Klebesadel et al. 1973) are the most violent stellar explosions in the universe. The duration of  $T_{90}$  is defined as the time corresponding to 5% – 95% of a burst fluence (Kouveliotou et al. 1993; Koshut et al. 1995; Hamburg & Goldstein 2016). Largely based on the parameter of  $T_{90}$ , the short and long GRBs classification sketch was established (Eichler et al. 1989) and intensive researches (Kouveliotou et al. 1993; Paczyński 1998; King et al. 2007; Řípa et al. 2012; Bystricky et al. 2012; Tarnopolski 2015b, 2016a,b,c; Zitouni et al. 2015, 2018; Ohmori et al. 2016; Zhang et al. 2016; Kulkarni & Desai 2017; Kwong & Nadarajah 2018) have shown that  $T_{90} \approx 2s$  is the critical duration of this classification. For the origin of GRBs, the mainstream view is that long Gamma-Ray Bursts (lGRBs) with a duration of  $T_{90} > 2s$  originate from the collapses of massive stars (Bloom et al. 1999; Matheson et al. 2003; Woosley 1993; Paczyński 1998; Wheeler et al. 2000), while short Gamma-Ray Bursts (sGRBs) with  $T_{90} < 2s$  come from double neutron star (NS-NS) or NS-black hole (BH) mergers (Eichler et al. 1989; Nakar 2007; Tanvir et al. 2013; Goldstein et al. 2017; Abbott et al. 2017). However, note that the possibility that some GRBs may be produced by other processes than the above two mechanisms still cannot be completely expelled yet. For example,

some events may be associated with the kick of high speed neutron stars (Huang et al. 2003; Xu et al. 2022). Consequently, there may also exist other kinds of GRBs. Examining the classification of GRBs can help reveal their trigger mechanisms.

The  $T_{90}$  duration was noticed early on to be composed of two lognormal functions (McBreen et al. 1994; Koshut et al. 1996; Kouveliotou et al. 1996). However, Horváth (1998) found a prominent third group between the classic short and long groups when studying the  $T_{90}$  data of 797 *CGRO/BATSE* GRBs, which means the emergence of the intermediate-duration class of GRBs. The third class was reconfirmed by different data sets from various detectors such as *Swift/BAT* (Horváth et al. 2008) and *Fermi/GBM* (Tarnopolski 2015a). Several authors (Huja & Řípa 2009; Zitouni et al. 2015; Zhang et al. 2016) analyzed those GRBs with measured redshifts in both the observer frame and the rest frame. They argued that the three Gaussian component model and the two Gaussian component model are almost equally suitable. de Ugarte Postigo et al. (2011) carefully analyzed the properties of the presumed intermediate GRBs and found that they differ from long GRBs only in having a lower luminosity, so that they might be simply a low-luminosity tail of the lGRB group (Bromberg et al. 2011). Also note that this intermediate GRBs may relate to short GRBs with extended emission (sGRBEE; Norris & Bonnell 2006; Dichiara et al. 2021), i.e., they have a duration that would make them being identified as long GRBs but without an associated supernova. They could most likely originate from the merger of a white dwarf with an NS (King et al. 2007) or BH (Dong et al. 2018).

\* E-mail: liang\_zhang\_gz@sina.com

† E-mail: j\_j\_luo@sina.com

‡ E-mail: hyf@nju.edu.cn

Further separation of long GRBs into subgroups was also considered. Horváth (2002) studied a large sample of 2041 *CGRO/BATSE* GRBs and found that the elusive third group seems to be blended into the long GRB group. A similar conclusion is also drawn by Tarnopolski (2015a). It is worth noting that Tarnopolski (2015b, 2019b) attributed this phenomenon to the skewness of the component. Tarnopolski (2015b) claimed that the logarithmic duration distribution need not necessarily be symmetrical. The asymmetry (skewness) can originate from, e.g., an asymmetric distribution of the progenitor envelope mass (Zitouni et al. 2015). Several authors (Tarnopolski 2016b,c; Kwong & Nadarajah 2018) have tested the skew distribution of *BATSE*, *Swift* and *Fermi* GRBs separately. It was found that the mixture of two skewed components are either significantly better than, or at least as good as, three-component symmetric models, indicating that the third class is unnecessary and could be discarded.

It has always been a controversial topic that GRBs can be classified into two components or else, by univariate analysis. A natural idea is to introduce bivariate analysis. Many studies have introduced the ratio of fluence in different bands, also known as hardness ratio (hereafter *HR*), as the second variable to study the classification of GRBs on the  $\log T_{90} - \log HR$  plane. However, different results are obtained by different groups. Mukherjee et al. (1998) and Horváth et al. (2006, 2010) argued that three Gaussian components are the optimal interpretation for GRBs on the  $\log T_{90} - \log HR$  plane, while Řípa et al. (2012), Zhang et al. (2016) and Narayana Bhat et al. (2016) suggested that two components are favored by the observational data. Very recently, Tarnopolski (2019a,b) used four kinds of bivariate distribution functions – normal, skew-normal, Student, skew-Student (hereafter  $\mathcal{N}$ ,  $\mathcal{SN}$ ,  $\mathcal{T}$ ,  $\mathcal{ST}$ , respectively) to fit the data sets of *CGRO/BATSE*, *Fermi/GBM*, *Swift/BAT*, *Konus-Wind*, *RHESSI*, *Suzaku/WAM* GRBs on the  $\log T_{90} - \log HR$  plane. The presence of two or three components varies from detector to detector. It should be emphasized that the motivation of introducing skewed distribution is due to the fact that the original data set itself might be skewed (Tarnopolski 2019a,b). In this case, modeling an inherently skewed distribution with a mixture of symmetric groups requires excessive components to be included, resulting in a spurious determination of the number of underlying classes (Koen & Bere 2012).

In previous studies, when skewed distribution functions are used to fit the observational data of different missions, the sample sizes are usually very limited, especially for *Fermi/GBM* and *Swift/BAT* GRBs (Tarnopolski 2019a,b). Here we follow Tarnopolski (2019a,b) to study the distribution and classification of GRBs on the  $T_{90} - HR$  plane for *CGRO/BATSE*, *Swift/BAT* and *Fermi/GBM* events, with the sample sizes significantly expanded. To increase the stability and credibility of the analysis, we also adopt the statistical bootstrap re-sampling method as done by Zhang et al. (2016).

Our paper is organized as follows. The data selection process is described in Section 2. Our statistical methods and the four bivariate distribution functions used in this study are introduced in Section 3. The main results are presented in Section 4. Finally, Section 5 is our conclusion and discussion.  $\mathbf{R}^1$  statistical language is utilized throughout the paper and the fittings of observational data points are performed with the  $\mathbf{R}$  package of *mixsmsn*<sup>2</sup> (Prates et al. 2013).

## 2 DATA SELECTION

We use three GRB samples in our study. These events are detected by *CGRO/BATSE*, *Swift*, and *Fermi*, respectively. Here we describe the three data sets as follows.

(i) The *CGRO/BATSE* catalogue<sup>3</sup> contains a total of 2702 GRBs. Among these events, 1954 events have valid  $T_{90}$ ,  $Fluence_2(50 - 100keV)$ ,  $Fluence_3(100 - 300keV)$  data, which are selected for our study. The *HR* is calculated as

$$HR = \frac{S_{100-300keV}}{S_{50-100keV}} = \frac{Fluence_3}{Fluence_2}. \quad (1)$$

(ii) The *Swift* satellite, dedicated to GRBs studies, was launched on 2004 November 20 (Gehrels et al. 2004; Butler et al. 2007; Jespersen et al. 2021). The *Swift/BAT* catalogue contains 1526 GRBs as of March 28, 2022<sup>4</sup>. However, it does not provide fluence values in the required energy bands needed to calculate the *HR* parameter. In fact *Swift* catalog contains fluence values, but only in one band from 15 to 150 keV. So, we use the optimal spectral fitting model to derive *HR*. When the optimal fitting model is a cutoff power-law (CPL) function, the corresponding  $E_{peak}$  value is then obtained from the GCN circular<sup>5</sup> <sup>6</sup>, such as in the cases of GRBs 220325A, 220101A, 211225b, etc. Finally, we obtained a sample of 1365 *Swift/BAT* GRBs with necessary parameters available. The parameter of *HR* is then calculated as

$$HR = \frac{S_{50-100keV}}{S_{15-25keV}} = \frac{\int_{50keV}^{100keV} F(E)E dE}{\int_{15keV}^{25keV} F(E)E dE}, \quad (2)$$

where  $f(E)$  corresponds to the best fit spectrum function which could be a power-law (PL) or CPL.

(iii) The *Fermi* satellite, dedicated to high energy phenomena and GRB studies, was launched in June, 2008 (Meegan et al. 2009). The *Fermi/GBM* catalogue (von Kienlin et al. 2020) contains 3255 GRBs as of March 28, 2022, which can be accessed through the HEASARC website<sup>7</sup>. Similar to the *Swift* GRB catalogue, the *Fermi* catalogue also does not provide required fluence data that could be directly used to calculate the hardness parameter. Again, we resort to the optimal spectral fitting model. The optimal spectral fittings are available for 2310 *Fermi* GRBs, of which the spectra are best fit by one of the four forms: power-law ('plaw'), Comptonized ('comp'), Band ('band') (Band et al. 1993a,b), and smoothly broken power law ('sbpl') (Ryde 1999). Using the spectrum, the *HR* parameter is then calculated as:

$$HR = \frac{S_{100-300keV}}{S_{25-50keV}} = \frac{\int_{100keV}^{300keV} F(E)E dE}{\int_{25keV}^{50keV} F(E)E dE}. \quad (3)$$

For the above three GRB samples, we have downloaded the duration data from the corresponding websites and calculated the *HR* parameter. Table 1 sums up the general features of our three data sets.

<sup>3</sup> <https://heasarc.gsfc.nasa.gov/W3Browse/cgro/batsegrb.html>

<sup>4</sup> [https://swift.gsfc.nasa.gov/archive/grb\\_table/](https://swift.gsfc.nasa.gov/archive/grb_table/)

<sup>5</sup> [https://gcn.gsfc.nasa.gov/gcn3\\_archive.html](https://gcn.gsfc.nasa.gov/gcn3_archive.html)

<sup>6</sup> <https://www.mpe.mpg.de/~jcg/grbgen.html>

<sup>7</sup> <https://heasarc.gsfc.nasa.gov/W3Browse/fermi/fermigbrst.html>

<sup>1</sup> <https://cran.r-project.org/>

<sup>2</sup> <https://cran.r-project.org/web/packages/mixsmsn/index.html>

**Table 1.** Basic features of the three GRB samples used in this study

Data Set Name	No. <sup>a</sup>	Source	Model <sup>b</sup>	Parameters <sup>c</sup>	Energy range (keV) <sup>d</sup>	Reference
<i>CGRO/BATSE</i>	1954 (2702)	<i>BATSE</i> catalogue	-	$T_{90}$ , fluence2, fluence3	100 — 300 , 50 — 100	e
<i>Swift/BAT</i>	1365 (1526)	<i>Swift</i> catalogue	PL CPL plaw	$T_{90}$ , index $T_{90}$ , index, Epeak $T_{90}$ , index	50 — 100 , 15 — 25	f, g
<i>Fermi/GBM</i>	2310 (3255)	<i>Fermi</i> catalogue	comp band sbpl	$T_{90}$ , index, Epeak $T_{90}$ , alpha, beta, Epeak $T_{90}$ , index1, brken, brksc, index2	300 — 100 , 50 — 25	h

<sup>a</sup> The number of GRBs used in this study (i.e. the number of GRBs having valid  $T_{90}$  and  $HR$  parameters. The number in the parentheses represents the total number of GRBs detected by each detector as of March 28, 2022.

<sup>b</sup> The optimal spectral fitting models available on the website. We use the optimal spectral fitting model to calculate the  $HR$  parameter when the required fluences are not directly available.

<sup>c</sup> Parameters involved in the optimal spectral fitting model.

<sup>d</sup> Energy ranges defined for calculating the  $HR$  parameter.

<sup>e</sup> website: <https://heasarc.gsfc.nasa.gov/W3Browse/cgro/batsegrb.html>

<sup>f</sup> website: [https://swift.gsfc.nasa.gov/archive/grb\\_table/](https://swift.gsfc.nasa.gov/archive/grb_table/)

<sup>g</sup> website: [https://gcn.gsfc.nasa.gov/gcn3\\_archive.html](https://gcn.gsfc.nasa.gov/gcn3_archive.html)

<sup>h</sup> website: <https://heasarc.gsfc.nasa.gov/W3Browse/fermi/fermigbrst.html>

### 3 METHOD

#### 3.1 Maximum likelihood Algorithm

For a given distribution, we denote the probability density function (hereafter PDF) as  $f(x; \theta)$ , where  $\theta = \{\theta_i\}_{i=1}^p$  is a set of parameters (Tarnopolski 2019b). The logarithmic likelihood function is:

$$\mathcal{L}_p(\theta) = \sum_{i=1}^N \ln f(x_i; \theta), \quad (4)$$

where  $\{x_i\}_{i=1}^N$  is the data sample based on which a distribution function is tested (Tarnopolski 2019b). The maximum likelihood (hereafter ML) algorithm (Bhattacharyya et al. 2022; Chromey & VERITAS Collaboration 2022) tries to find the largest probability value. Therefore, the goal is to find a set of  $\hat{\theta}$  to maximize the likelihood function, i.e.,  $\mathcal{L}_{p,max} \equiv \mathcal{L}_p(\hat{\theta})$ .

#### 3.2 Four Mixed Bivariate Distributions

The total PDF of a mixture of  $n$  components, each having a PDF given by  $f_i(x; \theta^{(i)})$ , is defined as

$$f(x; \theta) = \sum_{i=1}^n A_i f_i(x; \theta^{(i)}), \quad (5)$$

where the weights  $A_i$  satisfies the relation of  $\sum_{i=1}^n A_i = 1$ ,  $\theta = \bigcup_{i=1}^n \theta^{(i)}$  (Tarnopolski 2019b). In this study, we consider four kinds of distributions, as described below.

The PDF of an  $\mathcal{N}$  distribution (Mudelsee 2014) is:

$$f^{\mathcal{N}}(x; \mu, \Sigma) = \frac{1}{2\pi\sqrt{|\Sigma|}} \exp\left[-\frac{1}{2}(x - \mu)^T \Sigma^{-1}(x - \mu)\right], \quad (6)$$

where  $\mu$  is the mean of the parameter set,  $|\Sigma| = \det(\Sigma)$ , and  $\Sigma$  is the covariance matrix, (Tarnopolski 2019b),

$$\Sigma = \begin{pmatrix} \sigma_x^2 & \rho\delta_x\sigma_y \\ \rho\delta_x\sigma_y & \sigma_y^2 \end{pmatrix}. \quad (7)$$

A mixture of  $n$  components is described by  $p = 6n - 1$  free parameters.

Similarly, the PDF of an  $\mathcal{SN}$  distribution (Azzalini 1986) is

$$f^{\mathcal{SN}}(x; \mu, \Sigma, \lambda) = 2f^{\mathcal{N}}(x; \mu, \Sigma) \Phi\left(\lambda^T \Sigma^{-1/2}(x - \mu)\right), \quad (8)$$

where  $\Phi$  represents the cumulative distribution function (CDF) of a univariate standard normal distribution,  $\lambda$  denotes the skewness parameter (Tarnopolski 2019b). A mixture of  $n$  components is described by  $p = 8n - 1$  free parameters.

The PDF of a  $\mathcal{T}$  distribution (Lange et al. 1989) is

$$f^{\mathcal{T}}(x; \mu, \Sigma, \nu) = \frac{1}{\pi\nu\sqrt{|\Sigma|}} \frac{\Gamma\left(\frac{\nu+2}{2}\right)}{\Gamma\left(\frac{\nu}{2}\right)} \times \left(1 + \frac{1}{\nu}(x - \mu)^T \Sigma^{-1}(x - \mu)\right)^{-\frac{\nu+2}{2}}, \quad (9)$$

where  $\nu$  is degrees of freedom (dof) and  $\Gamma$  is the gamma function.  $\mu$  is the mean of the  $\mathcal{T}$  distribution, and the covariance matrix is  $\frac{\nu}{\nu-2}\Sigma$  (Tarnopolski 2019b). A mixture of  $n$  components is described by  $p = 6n$  free parameters.

The PDF of an  $\mathcal{ST}$  distribution is (Azzalini & Capitanio 2003)

$$f^{\mathcal{ST}}(x; \mu, \Sigma, \nu, \lambda) = 2f^{(\mathcal{T})}(x; \mu, \Sigma, \nu) \times T_{\nu+2}\left(\sqrt{\frac{\nu+2}{\nu+(x-\mu)^T \Sigma^{-1}(x-\mu)}} \lambda^T \Sigma^{-1/2}(x-\mu)\right), \quad (10)$$

where  $T_{\nu+2}$  represents the CDF of the standard bivariate student distribution,  $\lambda$  is the skewness parameter vector. A mixture of  $n$  components is described by  $p = 8n$  free parameters.

Table 2 presents the number of free parameters for the above four distributions, from which we could clearly see the complexity of each distribution.

#### 3.3 The Criteria for Model Selection

As is mentioned in Section 3.1, using the ML algorithm, one can obtain the best PDF for the observational data by assuming a mixture

**Table 2.** The number of free parameters in the four distributions.

Model name	No. of free parameters <sup>a</sup>
$\mathcal{N}$	$6n - 1$
$\mathcal{SN}$	$8n - 1$
$\mathcal{T}$	$6n$
$\mathcal{ST}$	$8n$

<sup>a</sup>  $n$  represents the number of mixed components.

of  $n$  components, with each component follows one of the four kinds of distributions:  $\mathcal{N}$ ,  $\mathcal{SN}$ ,  $\mathcal{T}$ ,  $\mathcal{ST}$ . Theoretically, it is always possible to increase the logarithmic likelihood value by introducing more free parameters (Tarnopolski 2019b), but note that additional parameters also indicate that the model might be too complicated. In general, the Akaike information criterion ( $AIC$ ) (Akaike 1974) and Bayesian information criterion ( $BIC$ ) (Schwarz 1978) are widely used as effective statistical criterions for model selection (Burnham & Anderson 2004; Biesiada 2007; Liddle 2007). Herein, the goal is to obtain the simplest possible model that could adequately describe the data, so we will adopt the  $BIC$  criterion. It takes the sample size into consideration to avoid over-fitting.

The  $BIC$  criterion is defined as

$$BIC = p \ln N - 2 \ln P_{max}, \quad (11)$$

where  $P_{max}$  is the  $ML$  achieved in modeling the data (Zhang et al. 2016).  $p$  is the number of free parameters of the model and  $N$  is the sample size.

The  $BIC$  method always chooses the model with the smallest value  $BIC_{min}$  as the best model (Zhang et al. 2016). To assess the goodness of other models, we can calculate their difference of  $BIC$  values with respect to the best model (Burnham & Anderson 2004),  $\Delta BIC_i = BIC_i - BIC_{min}$ . If  $\Delta BIC_i < 2$ , then there is also substantial support for the  $i$ th model and the possibility that it is also a proper description is high. When  $2 < \Delta BIC_i < 6$ , then there is significant evidence against the  $i$ th model. When  $6 < \Delta BIC_i < 10$ , the evidence of rejection is further enhanced. Finally, models with  $\Delta BIC_i > 10$  yield very strong evidence against the  $i$ th model (essentially rejected; (Burnham & Anderson 2004; Biesiada 2007; Zhang et al. 2016)).

### 3.4 Bootstrap Re-sampling Method

The bootstrap re-sampling method (Özel & Mayer-Hasselwander 1985) is a powerful statistical tool to quantify the uncertainty associated with a given estimator or statistical learning method. It repeatedly draws samples from a training data set and refits a given model on each sample with the goal of learning more about the model. Zhang et al. (2016) used this methodology to eliminate the contingency and deviation of their numerical results. Herein, the bootstrap re-sampling method will also be used to stabilize the  $BIC$  information outputs of the four models, so as to determine the distribution and classification of the GRBs observed by the three detectors.

### 3.5 Data Analysis Process

We use the function `smsn.mmix()` in the  $R$  package `mixsmsn` to fit the data sets. This function is responsible for the implementation of the expectation-maximization (EM) algorithm for the multivariate models, as explained in Section 3.2. Note that the initial value is set by `kmeans` randomly, so EM algorithm may converge to different values in each optimization calculation, resulting in some different

$BIC$  values. To overcome this problem, we use the bootstrap re-sampling method to stabilize the output  $BIC$  values.

## 4 RESULTS

### 4.1 Fitting results

In this study, the initial parameters are set as:  $\mu = NULL$ ,  $\Sigma = NULL$ ,  $shape = NULL$ ,  $pii = NULL$  and `get.init = TRUE`. It means that the initial values of the EM algorithm are obtained using a combination of the  $R$  function `kmeans` and the moment method. We further set `error = 0.0001`, which corresponds to the stopping criterion for the EM algorithm. For more details, please see Basso et al. (2010).

For the three GRB samples detected by *CGRO/BATSE*, *Swift/BAT*, and *Fermi/GBM*, we have applied the above methods to examine how many classes may exist among them. We test the four kinds of distribution for each class on the  $\log T_{90} - \log HR$  plane, i.e.,  $\mathcal{N}$ ,  $\mathcal{SN}$ ,  $\mathcal{T}$ ,  $\mathcal{ST}$ . The number of mixed components, i.e. classes, ranges from 1 to 5. Table 3 presents all the  $BIC$  values, together with the minimum value of  $BIC_{min}$  which indicates the optimal fitting model for the data set.

From Table 3, it can be seen that all three samples support a symmetrical distribution ( $\mathcal{N}$  or  $\mathcal{T}$ ) both for 1 time and  $10^4$  times fitting, which generally has a smaller  $BIC$  as compared with skewed distributions ( $\mathcal{SN}$  or  $\mathcal{ST}$ ). At the same time, we could also see that the number of components should generally be two or three, since the  $BIC$  values are much higher when the component number is taken as 1, 4, or 5.

For the *CGRO/BATSE* sample, the preferred distribution is  $\mathcal{T}$ , with three components, both for 1 time and  $10^4$  times fitting. For *Swift/BAT* GRBs, the optimal distribution is  $\mathcal{N}$ , with three components, both for 1 time and  $10^4$  times fitting. For *Fermi/GBM* events, the optimal distribution is  $\mathcal{N}$  both for both 1 time and  $10^4$  times fitting. Note that the 1 time fitting prefers two components while  $10^4$  times fitting prefers three components.

However, it is worth mentioning that the difference in  $BIC$  is only  $\Delta BIC_{2\mathcal{N}-3\mathcal{N}} = -1.968$  (5.317 for  $10^4$  times fitting) for 1 time fitting. When the number of free parameters (as is shown in Table 2; indicating the complexity of the model) of the fitting model ( $3\mathcal{N}$  is 17,  $2\mathcal{N}$  is 11) is considered, it is hard to say that the three component classification scheme is better than the two component classification scheme.

Additionally, from Table 3, we could see that the second best fitting distribution is  $\mathcal{N}$ ,  $\mathcal{T}$ ,  $\mathcal{T}$  for *CGRO/BATSE*, *Swift/BAT*, *Fermi/GBM* GRBs, respectively, while the asymmetric distributions ( $\mathcal{SN}$ ,  $\mathcal{ST}$ ) are generally unsupported.

Fig.1 shows the results of 1 time and  $10^4$  times fitting for the *CGRO/BATSE* data set. It can be seen that the profiles of 1 time fitting and  $10^4$  times fitting are quite similar, but the  $BIC$  of  $10^4$  times fitting is generally significantly lower. We could also see that for the 1 time fitting,  $3\mathcal{T}$  is the optimal fitting model, while  $3\mathcal{N}$  is the second optimal fitting model. For the  $10^4$  times fitting,  $3\mathcal{N}$  becomes the optimal model while  $3\mathcal{T}$  becomes the second optimal model. In all the cases, the  $\mathcal{SN}$  and  $\mathcal{ST}$  distribution (skewed models) can be safely expelled since their  $BIC$  values are obviously too high.

Fig.2 illustrates the 1 time and  $10^4$  times fitting results by the optimal  $3\mathcal{T}$  model for *CGRO/BATSE* GRBs. There are three contour curves in this figure, which are the full width at half maximum (hereafter  $FWHM$ ) for each component. The blue contour includes traditional short GRBs, which are located to the left of  $T_{90} = 2$  s

**Table 3.** A direct comparison of  $BIC$  between the 1 time fitting results and the  $10^4$  times fitting results for the three GRB samples.

Detector	Bootstrap time	Component	$BIC_{min}^a$	$\Delta BIC (BIC - BIC_{min})$ of four models			
				$N$	$SN$	$\mathcal{T}$	$\mathcal{ST}$
<i>CGRO/BATSE</i>	1	1	4848.189	756.463	354.644	727.414	299.48
		2		67.624	87.654	8.622	4.592
		3		6.477	40.444	0	45.911
		4		42.670	91.662	35.746	109.456
		5		83.043	161.680	74.808	151.307
	$10^4$	1	4831.242	763.845	481.017	737.251	309.055
		2		63.771	72.380	14.217	19.377
		3		1.316	38.882	0	40.518
		4		34.032	89.507	29.415	90.180
		5		33.482	128.119	57.442	131.919
<i>Swift/BAT</i>	1	1	2592.555	418.816	179.351	324.3	124.69
		2		46.584	69.711	56.473	80.434
		3		0	32.961	8.865	42.884
		4		33.504	81.405	39.720	89.291
		5		62.798	130.388	70.898	137.69
	$10^4$	1	2576.229	428.414	218.094	336.370	133.266
		2		52.007	71.233	63.959	79.556
		3		0	25.210	10.363	32.960
		4		25.840	65.535	34.969	73.801
		5		50.677	105.976	60.654	112.524
<i>Fermi/GBM</i>	1	1	5549.238	679.57	193.943	658.199	188.664
		2		0	38.93	5.614	43.499
		3		1.968	56.071	10.755	61.587
		4		47.963	109.429	57.018	119.216
		5		85.793	153.794	95.489	160.772
	$10^4$	1	5532.556	690.352	253.377	668.223	195.384
		2		5.317	40.859	10.992	42.924
		3		0	50.790	10.148	56.376
		4		32.626	90.584	42.454	89.937
		5		65.993	132.932	66.188	128.966

Note: for the  $10^4$  times fitting,  $BIC$  is the average value of all the calculations.

<sup>a</sup> The minimum value of  $BIC$  for all the calculations.

line, with a relatively large  $HR$  value. The red contour contains most of the traditional long GRBs with  $T_{90} = 2$  s and with a relatively smaller  $HR$ . The green contour shows the intermediate component. Note that most GRBs included in this component have a duration of  $T_{90} > 2$  s, and their  $HR$  value is also small. It means that these GRBs are quite similar to traditional long GRBs. The third row of Table 4 presents the number of GRBs included in each component for the left panel of Fig.2. We see that the number of GRBs in each component (short, intermediate, long GRBs) is 500, 385 and 1069, respectively. It should also be noted that the GRBs in the intermediate component only account for a ratio of 26.479% of all long GRBs, as could be seen from Table 4. So, the intermediate GRBs, if exists, is only a small group.

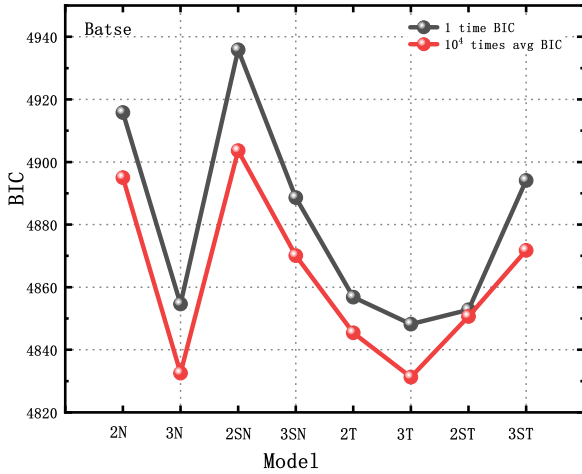
Fig.3 shows the 1 time and  $10^4$  times fitting results for the *Swift/BAT* GRB data set. Similar to Fig.1, we see that the profiles of 1 time fitting and  $10^4$  times fitting are quite alike, with the  $BIC$  of  $10^4$  times fitting significantly lower. Fig.3 clearly shows that  $3N$  is the optimal fitting model, while  $3\mathcal{T}$  is the second optimal fitting model. The distribution of  $SN$  and  $\mathcal{ST}$  can be essentially expelled due to large  $BIC$  values.

Fig.4 illustrates the 1 time and  $10^4$  times fitting results by the optimal  $3N$  model for *Swift/BAT* GRBs. Again, there are three contour curves in Fig.4, which are the  $FWHM$  for each component. The blue contour includes traditional short GRBs. The red contour contains most of the traditional long GRBs. The green contour shows the intermediate component. Again, most GRBs of this component

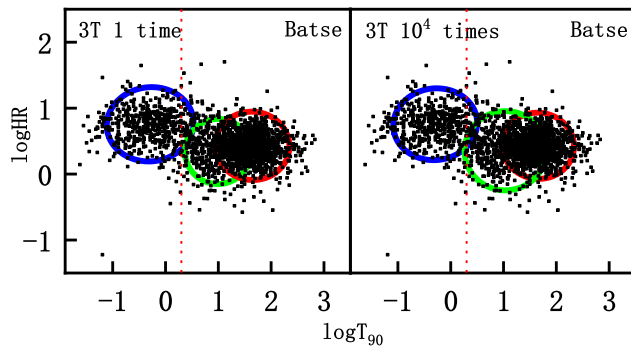
are quite similar to traditional long GRBs, and the number of events is small. From the fourth row of Table 4, it can be seen that the number of GRBs in each component (short, intermediate, long GRBs) is 92, 507 and 766 respectively. GRBs in the intermediate component only account for a ratio of 39.827% of all long GRBs, as shown in Table 4. Note that this ratio is the largest among all the three data sets.

Fig.5 shows the 1 time and  $10^4$  times fitting results for the *Fermi/GBM* GRB data set. Again, the profiles of 1 time fitting and  $10^4$  times fitting are quite similar, with the  $BIC$  of  $10^4$  times fitting significantly lower. In Fig.5, we see that  $3N$  is the optimal fitting model, and  $3\mathcal{T}$  is the second optimal fitting model. The distribution of  $SN$  and  $\mathcal{ST}$  can be safely ruled out since the corresponding  $BIC$  values are large.

Fig.6 presents the results of optimal  $2N$  model for 1 time fitting, and optimal  $3N$  model for  $10^4$  times fitting, for *Fermi/GBM* GRBs. As a result, there are two contour curves in the left panel and three contour curves in the right panel of Fig.6. The blue contour mainly includes short GRBs. The red contour contains most of the long GRBs. The green contour in the right panel corresponds to the intermediate component, which are also long GRBs. Similar to *CGRO/BATSE* events, the number of GRBs in this group is small. The first and second row of Table 4 shows the number of GRBs in each component of Fig.6. In the left panel of Fig.6, 461 and 1849 GRBs are included in the short GRB group and long GRB group, respectively. In the right panel, there are 419, 625, 1266 GRBs in the three groups, respectively. Again, we see that GRBs in the inter-



**Figure 1.** *BIC* values of 1 time and  $10^4$  times fitting results for the *CGRO/BATSE* data set. The X-axis represents different models and the corresponding number of mixed components. The Y-axis represents *BIC* values. The grey line corresponds to 1 time fitting, while the red line shows the average *BIC* of  $10^4$  times fitting results.



**Figure 2.** Fitting results of the *CGRO/BATSE* data with the optimal model of  $3\mathcal{T}$ . Both the X-axis and Y-axis are in logarithmic coordinates. The left panel shows the 1 time fitting *FWHM* of each component, and the right panel correspondingly shows the  $10^4$  times fitting result. The red dashed line represents  $T_{90} = 2$  s. The contour of the middle component overlaps severely with the contour of long GRBs, but is well separated from short GRBs, with little overlap.

mediate component only account for a ratio of 33.051% of all long GRBs, as shown in Table 4.

#### 4.2 Weakness in the above direct analysis

In the previous section, we have studied three GRB samples observed by three detectors, examining the possibility that there might be multiple groups (from 1 to 5 components) of GRBs. For each component, we assume that it could be one of the following four distributions:  $N$ ,  $SN$ ,  $\mathcal{T}$ ,  $ST$ . It is found that the optimal fitting results prefer symmetric distributions ( $\mathcal{T}$  or  $N$ ). For *CGRO/BATSE* and *Swift/BAT* GRBs, the results support that there are 3 components. But for *Fermi/GBM* GRBs, the difference in *BIC* for 2 components and 3 components is very small so that both possibilities could exist.

However, it should be noted that there some complicated factors in the three GRB samples, which might prevent us from drawing a firm conclusion directly from the observational data:

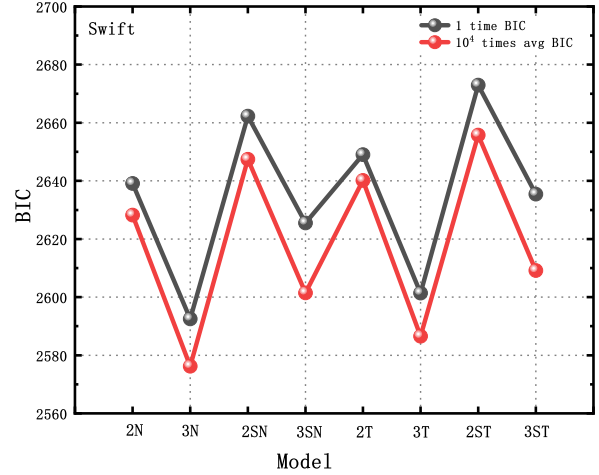


**Figure 3.** *BIC* values of 1 time and  $10^4$  times fitting results for the *Swift/BAT* data set. The X-axis represents different models and the corresponding number of mixed components. The Y-axis represents *BIC* values. The grey line corresponds to 1 time fitting, while the red line shows the average *BIC* of  $10^4$  times fitting results. Note that the  $3N$  model gives the minimum *BIC* value, thus presents the best fit.

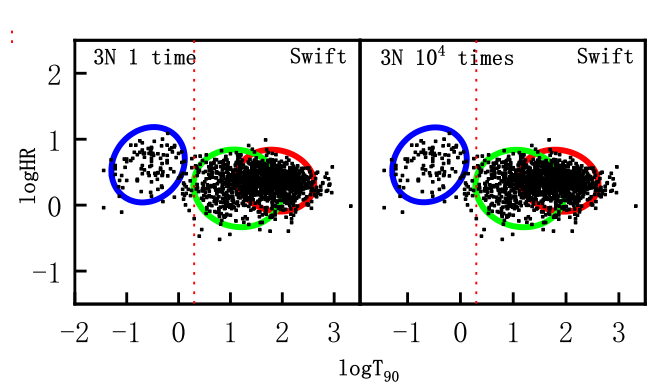


**Figure 4.** Fitting results of the *Swift/BAT* data with the optimal model of  $3N$ . Both the X-axis and Y-axis are in logarithmic coordinates. The left panel shows the 1 time fitting *FWHM* of each component, and the right panel correspondingly shows the  $10^4$  times fitting result. The red dashed line represents  $T_{90} = 2$  s. The contour of the middle component overlaps severely with the contour of long GRBs, but is well separated from short GRBs, with little overlap.

(i) The three detectors work in different energy bands (Tarnopolski 2019b), which may lead to different duration of  $T_{90}$  even for the same event. The derived *HR* parameter also may have different physical meanings.

(ii) The three detectors have different technical parameters, such as the field of view, signal to noise ratio, sensitivity (Tarnopolski 2019b). These may also lead to significant systematic difference in the three samples.

(iii) For each detector, the sample size (i.e. the number of GRBs contained in the data set) is also different from each other. This may have an impact on the GRB classification analysis (Horváth 1998, 2002; Tarnopolski 2015b, 2019b).

Both Factor (i) and Factor (ii) are connected to the selection effect of instruments and observations. They can significantly affect the classification of GRBs (Qin 2013). To overcome this problem, we need to know the intrinsic wide band spectra of GRBs as well

**Table 4.** Number of GRBs in each component for all the three samples, under the optimal distribution model.

Detector	Total No.	GRBs with $T_{90} < 2s$	left No. <sup>a</sup>	middle No. <sup>a</sup>	right No. <sup>a</sup>	ratio1 <sup>b</sup>	ratio2 <sup>b</sup>	ratio3 <sup>b</sup>
<i>Fermi</i> / <i>GBM</i> (2 <i>N</i> )	2310	372	461	-	1849	123.925%	-	100%
<i>Fermi</i> / <i>GBM</i> (3 <i>N</i> )	2310	372	419	625	1266	112.634%	33.051%	66.949%
<i>CGRO</i> / <i>BATSE</i> (3 <i>T</i> )	1954	466	500	385	1069	107.296%	26.479%	73.521%
<i>Swift</i> / <i>BAT</i> (3 <i>N</i> )	1365	118	92	507	766	77.966%	39.827%	60.173%

<sup>a</sup> The left No. counts the number of GRBs included in the blue *FWHM* contour in the left panel of Fig.2, Fig.4, Fig.6; The middle No. counts that included in the green *FWHM* contour; The right No. counts those included in the red *FWHM* contour.

<sup>b</sup> ratio1 =  $\frac{\text{leftNo.}}{\text{No. of GRBs with } T_{90} < 2s}$ , ratio2 =  $\frac{\text{middleNo.}}{\text{middleNo.} + \text{rightNo.}}$ , ratio3 =  $\frac{\text{rightNo.}}{\text{middleNo.} + \text{rightNo.}}$ .

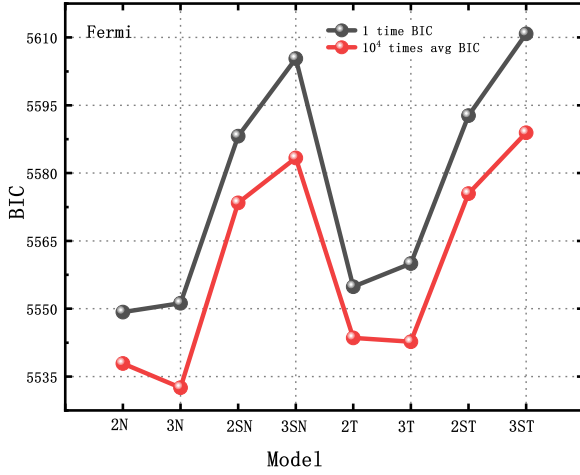


**Figure 5.** *BIC* values of 1 time and  $10^4$  times fitting results for the *Fermi*/*GBM* data set. The X-axis represents different models and the corresponding number of mixed components. The Y-axis represents *BIC* values. The grey line corresponds to 1 time fitting, while the red line shows the average *BIC* of  $10^4$  times fitting results. Note that the 2*N* model gives the minimum *BIC* value for 1 time fitting, while the 3*N* model gives the minimum *BIC* for  $10^4$  times fitting.

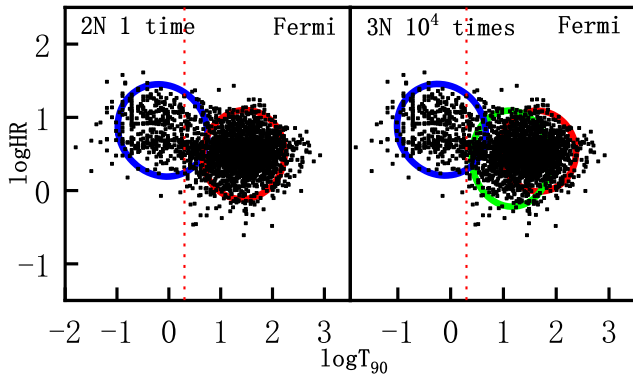


**Figure 6.** Fitting results of the *Fermi*/*GBM* data with optimal model of 2*N* (for 1 time fitting) or 3*N* (for  $10^4$  times fitting). Both the X-axis and Y-axis are in logarithmic coordinates. The left panel shows the 1 time fitting *FWHM* of each component, and the right panel correspondingly shows the  $10^4$  times fitting result. The red dashed line represents  $T_{90} = 2s$ . In the right panel, the contour of the middle component overlaps severely with the contour of long GRBs, but is well separated from short GRBs, with little overlap.

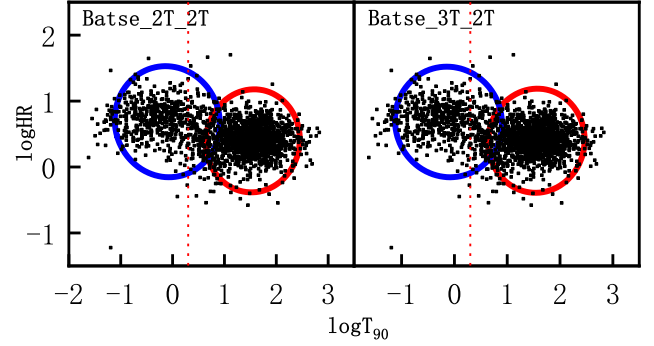


**Figure 7.** Illustration of our best fit to the mock *CGRO*/*BATSE* sample (sample size now expanded to 3255 GRBs) with the 2*T* model. Both the X-axis and Y-axis are in logarithmic coordinates. In the left panel, the 3255 mock GRBs are generated by assuming a 2*T* distribution. In the right panel, the 3255 mock GRBs are generated by assuming a 3*T* distribution. In both panels, the mock GRBs are finally best fit by the 2*T* distribution after  $10^4$  times bootstrap analysis, as shown by the blue and red *FWHM* contours. In this figure, the black scatter points correspond to the real GRBs detected by *CGRO*/*BATSE*. The red dashed line represents  $T_{90} = 2s$ .

as detailed response characteristics of each instruments, which is beyond the scope of this study. Here we will mainly concentrate on Factor (iii). The sample size may also affect our conclusion on the classification. Horváth (1998) investigated an early version of *BATSE* GRB catalogue, which contains 797 events. They found a prominent third peak, between the short and long groups, in the log  $T_{90}$  distribution, and hence claimed the existence of an intermediate-duration class of GRBs. Later, when an updated *BATSE* catalogue that contains 1929 events was re-analyzed, it was found that the intermediate peak almost disappears (Horváth 2002; Tarnopolski 2015b, 2019b). Tarnopolski (2019b) argued that it may be due to the skewness of the distribution of long GRBs.

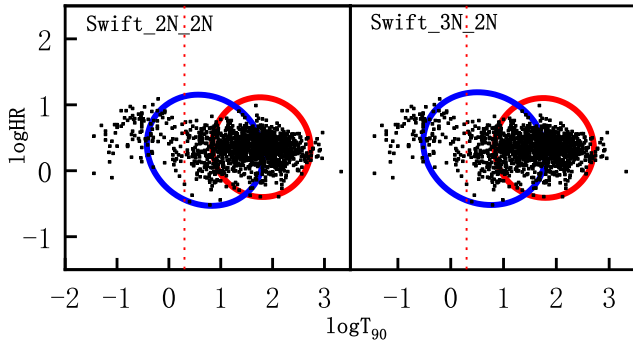
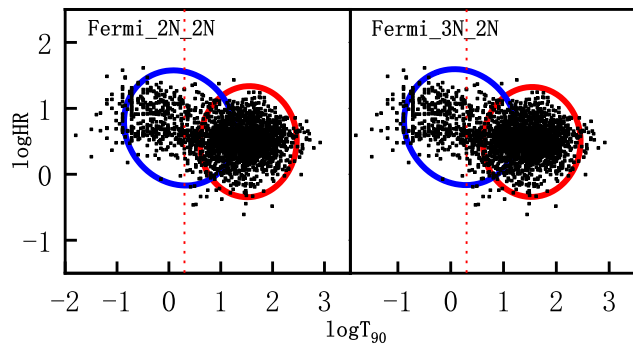
We notice that the three sample sizes are 1365, 1954, 2310, respectively. With the increasing of the sample size, the *BIC* difference between two component fitting and three component fitting becomes smaller, which are  $\Delta BIC_{2N(T)-3N(T)} = 46.584, 8.622, -1.968$  in the 1 time fitting case, as shown in Table 3. It clearly indicates that the classification scheme may be seriously affected by the sample size: when the sample size is small, the intermediate component may appear; but when the sample size becomes large, the intermediate component seems to disappear and merge with long GRBs. To overcome the problem induced by the limiting sample size (Factor iii), we will use the Bootstrap resampling method (Zhang et al. 2016) to construct some meaningful large samples, based on which we could further investigate the classification of GRBs in detail.

**Table 5.** *BIC* values of the expanded samples generated through the bootstrap re-sampling method. The sample size has been expanded to 3225 GRBs for each detector.

Detector	Resample of 2 $\mathcal{T}$ ( $N$ )		$\Delta BIC < 0^a$	Resample of 3 $\mathcal{T}$ ( $N$ )		$\Delta BIC < 0^a$
	2 $\mathcal{T}$ ( $N$ )	3 $\mathcal{T}$ ( $N$ )		2 $\mathcal{T}$ ( $N$ )	3 $\mathcal{T}$ ( $N$ )	
<i>CGRO/BATSE</i>	14560.829	14606.858	10000	14300.49	14340.361	9958
<i>Fermi/GBM</i>	13692.152	13733.845	9990	13573.818	13611.664	9972
<i>Swift/BAT</i>	12571.067	12615.573	9986	12603.524	12633.937	9608

Note: For the  $10^4$  times fitting, the *BIC* here is the average value.

<sup>a</sup>  $\Delta BIC = BIC_{2N(\mathcal{T})} - BIC_{3N(\mathcal{T})}$ . This column counts the number of fitting times that prefers the two components scheme over the three components scheme, after a total of  $10^4$  times fitting.

**Figure 8.** Illustration of our best fit to the mock *Swift/BAT* sample (sample size now expanded to 3255 GRBs) with the 2 $N$  model. Both the X-axis and Y-axis are in logarithmic coordinates. In the left panel, the 3255 mock GRBs are generated by assuming a 2 $N$  distribution. In the right panel, the 3255 mock GRBs are generated by assuming a 3 $N$  distribution. In both panels, the mock GRBs are finally best fit by the 2 $N$  distribution after  $10^4$  times bootstrap analysis, as shown by the blue and red *FWHM* contours. In this figure, the black scatter points correspond to the real GRBs detected by *Swift/BAT*. The red dashed line represents  $T_{90} = 2$  s.**Figure 9.** Illustration of our best fit to the mock *Fermi/GBM* sample (sample size now expanded to 3255 GRBs) with the 2 $N$  model. Both the X-axis and Y-axis are in logarithmic coordinates. In the left panel, the 3255 mock GRBs are generated by assuming a 2 $N$  distribution. In the right panel, the 3255 mock GRBs are generated by assuming a 3 $N$  distribution. In both panels, the mock GRBs are finally best fit by the 2 $N$  distribution after  $10^4$  times bootstrap analysis, as shown by the blue and red *FWHM* contours. In this figure, the black scatter points correspond to the real GRBs detected by *Fermi/GBM*. The red dashed line represents  $T_{90} = 2$  s.**Table 6.** Ratio of short GRBs in each sample.

Detector	total No.	No. of short GRBs	Ratio of short GRBs
<i>CGRO/BATSE</i>	1954	466	23.8%
<i>Fermi/GBM</i>	2310	372	16.1%
<i>Swift/BAT</i>	1365	118	8.6%

### 4.3 Bootstrap resampling analysis

The bootstrap analysis is done in the following steps:

(i) Expand the number of GRBs detected by a particular detector to 3255 events. To do so, we use the optimal distribution function ( $\mathcal{T}$  for *BATSE*;  $N$  for *Swift* and *Fermi*) and assume that the optimal classification scheme is either two components or three components. Following the optimal distribution function, we can randomly generate 3255 mock GRBs. This process is usually referred to as re-sampling. Note that 3255 is simply the number of GRBs detected by *Fermi/GBM* as of March 28, 2022 (see the HEASARC website), which is the largest sample size for GRBs detected by the three detectors. In our simulations, we set 3255 as the destination sample size.

(ii) With the mock GRB sample, using two component model and three component model to fit it to see which model presents a better result. We use 2 $\mathcal{T}$  and 3 $\mathcal{T}$  to fit the mock *BATSE* sample, and use 2 $N$  and 3 $N$  to fit the mock samples of *Swift* and *Fermi* detectors.

(iii) Repeat step (i) and (ii) for  $10^4$  times, and count the number of times that the mock samples are divided into two components and three components separately.

The *BIC* values of the mock samples are displayed in Table 5. The best fit results are illustrated in Fig.7 — Fig.9. From Table 5 and the figures, we find that for the mock *BATSE* samples generated from 2 $\mathcal{T}$  model, 100% of them are again better fit by the 2 $\mathcal{T}$  distribution. For the mock *Fermi* samples generated from 2 $N$  model, 99.9% of them are again better fit by the 2 $N$  distribution. For the mock *Swift* samples generated from 2 $N$  model, 99.86% of them are again better fit by the 2 $N$  distribution.

On the other hand, for the mock *BATSE* samples generated from 3 $\mathcal{T}$  model, 99.58% of them are better fit by the 2 $\mathcal{T}$  distribution. For the mock *Fermi* samples generated from 3 $N$  model, 99.72% of them are better fit by the 2 $N$  distribution. For the mock *Swift* samples generated from 3 $N$  model, 96.08% of them are again better fit by the 2 $N$  distribution. We see that after expanding the sample to 3225 GRBs, even though the mock GRBs are originally assumed to follow 3-component distribution, the sample finally is still better described by a 2-component classification. It strongly indicates that a large sample size tend to support a two-component scheme.

As shown in Fig.7 and Fig.9, the *FWHM* contours derived from



the bootstrap analysis can well identify the two components in the sample on the  $\log T_{90} - \log HR$  plane for mock GRBs of *BATSE* and *Fermi* detectors. However, in Fig.8, the blue contour seems to obviously deviate from the short component. As a result, many short *Swift* bursts are outside the contour circle. This may be due to the fact that the number of short GRBs is relatively small in the *Swift* sample, resulting in a low fitting weight. Table 6 lists the ratios of short GRBs in each sample. For *BATSE* GRBs, the number of short bursts is 466, accounting for 23.8% of the total events. For the *Fermi* sample, there are 372 short bursts and the ratio is 16.1%. But in the *Swift* sample, these are only 118 short events, which corresponds to a small ratio of 8.6%.

## 5 CONCLUSION

In this study, we investigate the distribution and classification of *BATSE*, *Swift* and *Fermi* GRBs. The possible existence of up to 5 components is carefully examined by using the Bayesian information criterion on the  $\log T_{90} - \log HR$  plane. For each component, the distribution could be one of the four forms:  $\mathcal{N}$ ,  $\mathcal{SN}$ ,  $\mathcal{T}$ , or  $\mathcal{ST}$ . Generally, all the three samples show a symmetric (either  $\mathcal{N}$  or  $\mathcal{T}$ ) distribution. For *CGRO/BATSE* and *Swift/BAT* data sets, the best fitting models are  $3\mathcal{T}$  and  $3\mathcal{N}$ , respectively. However, for the *Fermi/GBM* sample,  $2\mathcal{N}$  is almost as good as  $3\mathcal{N}$ . It is also found that the sample size has a great impact on the classification. When the sample size is large, the best classification scheme universally tends to two, instead of three as in the small sample size cases. A further bootstrap re-sampling analysis strongly supports this result.

Tarnopolski (2019a,b) have used a mixture of 2 — 3 components of  $\mathcal{N}$ ,  $\mathcal{SN}$ ,  $\mathcal{T}$ ,  $\mathcal{ST}$  to fit the data sets of *CGRO/BATSE*, *Fermi/GBM*, *Swift/BAT*, *Konus - Wind*, *RHESSI*, *Suzaku/WAM* on the  $\log T_{90} - \log HR$  plane. They argued that the  $2\mathcal{ST}$  model is better in describing the *CGRO/BATSE* and *Fermi/GBM* data sets under both *AIC* and *BIC* criteria (Tarnopolski 2019b). For *Swift*, they claimed that the *BIC* criteria prefers  $2\mathcal{ST}$  or  $2\mathcal{SN}$ , while the *AIC* prefers  $3\mathcal{ST}$  or  $3\mathcal{SN}$  (Tarnopolski 2019a).

For the *CGRO/BATSE* detector, we have adopted the same data set as Tarnopolski (2019b), but drawn a different conclusion on the skewness of the distribution (our  $10^4$  times fitting results prefer  $2\mathcal{T}$ , as compared with their  $2\mathcal{ST}$ ). We notice that Tarnopolski (2019b) carried out their studies mainly based on 1 time fitting, which may lead to significant random fluctuations. In fact, from Table 3, we could find that our 1 time fitting result of *CGRO/BATSE* is somewhat similar to that of Tarnopolski (2019b):  $2\mathcal{ST}$  is also a good fit, which is only slight worse than the best fitting model of  $3\mathcal{T}$ . In this study, we have further conducted  $10^4$  times fitting analysis, which can effectively overcome the fluctuations. We see that after  $10^4$  bootstrap re-sampling and fitting, the best fitting model is  $2\mathcal{T}$ .

As for *Fermi/GBM* and *Swift/BAT* data sets, the difference between our results and that of Tarnopolski (2019a,b) may be caused by several factors. First, the sample size is different, and our sample sizes are larger. The *Fermi/GBM* data set contains merely 1376 GRBs in Tarnopolski (2019b), but it is 2310 in this study. Similarly, the *Swift/BAT* data set contains 1033 events in Tarnopolski (2019a), and it is 1365 in our work. Second, the *HR* parameter is calculated by different method. In our study, this parameter is derived by using the optimal spectral fitting model. Thirdly, as mentioned above, we use the  $10^4$  times fitting analysis to overcome the fluctuations caused by 1 time fitting method. Our results on these two data sets further strengthen the conclusion that a symmetric distribution ( $\mathcal{N}$  or  $\mathcal{T}$ ) is

better than an asymmetric distribution ( $\mathcal{SN}$  or  $\mathcal{ST}$ ) for the currently observed GRBs on the  $T_{90} - HR$  plane.

A symmetric lognormal distribution ( $\mathcal{N}$  and  $\mathcal{T}$ ) may originate from realistic processes involving a number of independent parameters which somewhat randomly distributed in particular ranges Durbin (1957); Shlesinger (1982). Many examples of lognormal distributions are observed in nature, such as the propagation of a laser beam in a turbulent atmosphere (Majumdar & Gamo 1982), the size of cumulus clouds in the atmosphere, the strength of terrestrial lightning, etc. Interestingly, for the soft gamma-ray repeating source of *SGR 1806-20*, the time intervals between bursts also follow a lognormal distribution (Hurley et al. 1994). Similarly, the symmetric lognormal distribution of GRBs may be interpreted in the framework of the collapsar scenario: the GRB duration may be determined by the ejected envelope mass which itself could follow a symmetric distribution (Zitouni et al. 2015). Accretion of the ejected envelope by the newly formed black hole may give birth to the GRB. In the future, more GRBs will be observed and the classification of them will be investigated in further detail.

## ACKNOWLEDGEMENTS

We thank the anonymous referee for helpful comments and suggestions. This study is supported by the National Natural Science Foundation of China (Grant Nos. 12233002, 11873030, 12041306, 12147103, U1938201), by the Youth Science & Technology Talents Development Project of Guizhou Education Department (No.KY[2022]098), by National SKA Program of China No. 2020SKA0120300, by the National Key R&D Program of China (2021YFA0718500), and by the science research grants from the China Manned Space Project with NO. CMS-CSST-2021-B11.

## DATA AVAILABILITY

No new data were generated or analysed in support of this research.

## REFERENCES

- Abbott B. P., et al., 2017, *ApJ*, 848, L12  
 Akaike H., 1974, *IEEE Transactions on Automatic Control*, 19, 716  
 Azzalini A., 1986, *Scandinavian Journal of Statistics*, 12, 171  
 Azzalini A., Capitanio A., 2003, *Journal of the Royal Statistical Society: Series B (Statistical)*, 65, 367  
 Band D., et al., 1993a, in *American Astronomical Society Meeting Abstracts* #182. p. 74.09  
 Band D., et al., 1993b, *ApJ*, 413, 281  
 Basso R. M., Lachos V. H., Cabral C. R. B., Ghosh P., 2010, *Computational Statistics & Data Analysis*, 54, 2926  
 Bhattacharyya S., Tiwari H., Bharadwaj S., Majumdar S., 2022, *MNRAS*, 513, L1  
 Biesiada M., 2007, *J. Cosmology Astropart. Phys.*, 2007, 003  
 Bloom J. S., et al., 1999, *Nature*, 401, 453  
 Bromberg O., Nakar E., Piran T., 2011, *ApJ*, 739, L55  
 Burnham K. P., Anderson D. R., 2004, *Sociological Methods & Research*, 33, 261  
 Butler N. R., Kocevski D., Bloom J. S., Curtis J. L., 2007, *ApJ*, 671, 656  
 Bystricky P., Meszaros A., Ripa J., 2012, in *Proceedings of the 21st Annual Conference of Doctoral Students - WDS 2012*. p. 129  
 Chromey A., VERITAS Collaboration 2022, in *37th International Cosmic Ray Conference*. 12-23 July 2021. Berlin. p. 768 (arXiv:2108.07840)  
 Dichiera S., et al., 2021, *ApJ*, 911, L28  
 Dong Y.-Z., Gu W.-M., Liu T., Wang J., 2018, *MNRAS*, 475, L101

- Durbin R. B. J., 1957, *Journal of the Royal Statistical Society*, 120, 481
- Eichler D., Livio M., Piran T., Schramm D. N., 1989, *Nature*, 340, 126
- Gehrels N., et al., 2004, *ApJ*, 611, 1005
- Goldstein A., et al., 2017, *ApJ*, 848, L14
- Hamburg R., Goldstein A., 2016, in Eighth Huntsville Gamma-Ray Burst Symposium. p. 4099
- Horváth I., 1998, *ApJ*, 508, 757
- Horváth I., 2002, *A&A*, 392, 791
- Horváth I., Balázs L. G., Bagoly Z., Ryde F., Mészáros A., 2006, *A&A*, 447, 23
- Horváth I., Balázs L. G., Bagoly Z., Veres P., 2008, *A&A*, 489, L1
- Horváth I., Bagoly Z., Balázs L. G., de Ugarte Postigo A., Veres P., Mészáros A., 2010, *ApJ*, 713, 552
- Huang Y. F., Dai Z. G., Lu T., Cheng K. S., Wu X. F., 2003, *ApJ*, 594, 919
- Huja D., Řípa J., 2009, *Baltic Astronomy*, 18, 311
- Hurley K. J., McBreen B., Rabbette M., Steel S., 1994, *A&A*, 288, L49
- Jespersen C. K., Severin J. B., Steinhardt C. L., Vinther J., Fynbo J. P. U., Selsing J., Watson D., 2021, *VizieR Online Data Catalog*, p. J/ApJ/896/L20
- King A., Olsson E., Davies M. B., 2007, *MNRAS*, 374, L34
- Klebesadel R. W., Strong I. B., Olson R. A., 1973, *ApJ*, 182, L85
- Koen C., Bere A., 2012, *MNRAS*, 420, 405
- Koshut T. M., Paciesas W. S., Kouveliotou C., van Paradijs J., Pendleton G. N., Fishman G. J., Meegan C. A., 1995, in *American Astronomical Society Meeting Abstracts #186*. p. 53.01
- Koshut T. M., Paciesas W. S., Kouveliotou C., van Paradijs J., Pendleton G. N., Fishman G. J., Meegan C. A., 1996, *ApJ*, 463, 570
- Kouveliotou C., Meegan C. A., Fishman G. J., Bhat N. P., Briggs M. S., Koshut T. M., Paciesas W. S., Pendleton G. N., 1993, *ApJ*, 413, L101
- Kouveliotou C., Koshut T., Briggs M. S., Pendleton G. N., Meegan C. A., Fishman G. J., Lestrade J. P., 1996, in Kouveliotou C., Briggs M. F., Fishman G. J., eds, *American Institute of Physics Conference Series Vol. 384, Gamma-ray Bursts: 3rd Huntsville Symposium*. pp 42–46, doi:10.1063/1.51695
- Kulkarni S., Desai S., 2017, *Ap&SS*, 362, 70
- Kwong H. S., Nadarajah S., 2018, *MNRAS*, 473, 625
- Lange K. L., Little R. J. A., Taylor J. M. G., 1989, *Journal of the American Statistical Association*, 84, 881
- Liddle A. R., 2007, *MNRAS*, 377, L74
- Majumdar A. K., Gamo H., 1982, *Applied Optics*, 21, 2229
- Matheson T., et al., 2003, *ApJ*, 599, 394
- McBreen B., Hurley K. J., Long R., Metcalfe L., 1994, *MNRAS*, 271, 662
- Meegan C., et al., 2009, *ApJ*, 702, 791
- Mudelsee M., 2014, *Correlation*. Springer International Publishing, Cham, pp 271–319, doi:10.1007/978-3-319-04450-7\_7, [https://doi.org/10.1007/978-3-319-04450-7\\_7](https://doi.org/10.1007/978-3-319-04450-7_7)
- Mukherjee S., Feigelson E. D., Jogesh Babu G., Murtagh F., Fraley C., Raftery A., 1998, *ApJ*, 508, 314
- Nakar E., 2007, *Phys. Rep.*, 442, 166
- Narayana Bhat P., et al., 2016, *ApJS*, 223, 28
- Norris J. P., Bonnell J. T., 2006, *ApJ*, 643, 266
- Ohmori N., et al., 2016, *PASJ*, 68, S30
- Özel M. E., Mayer-Hasselwander H., 1985, in di Gesu V., Scarsi L., Crane P., Friedman J. H., Levialdi S., eds, *Data Analysis in Astronomy*. p. 81
- Paczyński B., 1998, *ApJ*, 494, L45
- Prates M. O., Lachos V. H., Barbosa Cabral C. R., 2013, *Journal of Statistical Software*, 54, 1–20
- Qin Y., 2013, *ApJ*, 763, 15
- Ryde F., 1999, *Astrophysical Letters and Communications*, 39, 281
- Schwarz G., 1978, *The Annals of Statistics*, 6, 461
- Shlesinger M. M. F., 1982, *Proceedings of the National Academy of Sciences of the United States of America*, 79, 3380
- Tanvir N. R., Levan A. J., Fruchter A. S., Hjorth J., Hounsell R. A., Wiersema K., Tunnicliffe R. L., 2013, *Nature*, 500, 547
- Tarnopolski M., 2015a, *Ap&SS*, 359, 20
- Tarnopolski M., 2015b, *A&A*, 581, A29
- Tarnopolski M., 2016a, *New Astron.*, 46, 54
- Tarnopolski M., 2016b, *Ap&SS*, 361, 125
- Tarnopolski M., 2016c, *MNRAS*, 458, 2024
- Tarnopolski M., 2019a, *Mem. Soc. Astron. Italiana*, 90, 45
- Tarnopolski M., 2019b, *ApJ*, 870, 105
- Wheeler J. C., Yi I., Höflich P., Wang L., 2000, *ApJ*, 537, 810
- Woosley S. E., 1993, *ApJ*, 405, 273
- Xu F., Geng J.-J., Wang X., Li L., Huang Y.-F., 2022, *MNRAS*, 509, 4916
- Zhang Z.-B., Yang E.-B., Choi C.-S., Chang H.-Y., 2016, *MNRAS*, 462, 3243
- Zitouni H., Guessoum N., Azzam W. J., Mochkovitch R., 2015, *Ap&SS*, 357, 7
- Zitouni H., Guessoum N., AlQassimi K. M., Alaryani O., 2018, *Ap&SS*, 363, 223
- de Ugarte Postigo A., et al., 2011, *A&A*, 525, A109
- Řípa J., Mészáros A., Veres P., Park I. H., 2012, *ApJ*, 756, 44
- von Kienlin A., et al., 2020, *ApJ*, 893, 46

This paper has been typeset from a  $\text{\TeX}/\text{\LaTeX}$  file prepared by the author.